

Role of the reactive sputtering deposition power in the phase control of cobalt oxide films

Nilton Francelosi Azevedo Neto, Douglas M. G. Leite, Paulo N. Lisboa-Filho, and José H. D. da Silva

Citation: *Journal of Vacuum Science & Technology A* **36**, 061512 (2018); doi: 10.1116/1.5046952

View online: <https://doi.org/10.1116/1.5046952>

View Table of Contents: <https://avs.scitation.org/toc/jva/36/6>

Published by the [American Vacuum Society](#)

ARTICLES YOU MAY BE INTERESTED IN

[Review Article: Atomic layer deposition for oxide semiconductor thin film transistors: Advances in research and development](#)

Journal of Vacuum Science & Technology A **36**, 060801 (2018); <https://doi.org/10.1116/1.5047237>

[Deposition of ZrON thin films by reactive magnetron sputtering using a hollow cylindrical target](#)

Journal of Vacuum Science & Technology A **36**, 061509 (2018); <https://doi.org/10.1116/1.5042439>

[Review Article: Stress in thin films and coatings: Current status, challenges, and prospects](#)

Journal of Vacuum Science & Technology A **36**, 020801 (2018); <https://doi.org/10.1116/1.5011790>

[Rapid atomic layer etching of Al₂O₃ using sequential exposures of hydrogen fluoride and trimethylaluminum with no purging](#)


Journal of Vacuum Science & Technology A **36**, 061508 (2018); <https://doi.org/10.1116/1.5043488>

[Precise control of ion and radical production using electron beam generated plasmas](#)

Journal of Vacuum Science & Technology A **36**, 060601 (2018); <https://doi.org/10.1116/1.5053615>

[Low-temperature homoepitaxial growth of two-dimensional antimony superlattices in silicon](#)

Journal of Vacuum Science & Technology A **36**, 061513 (2018); <https://doi.org/10.1116/1.5040837>



Instruments for Advanced Science


Contact Hiden Analytical for further details:
W www.HidenAnalytical.com
E info@hiden.co.uk

CLICK TO VIEW our product catalogue




Gas Analysis

- dynamic measurement of reaction gas streams
- catalysis and thermal analysis
- molecular beam studies
- dissolved species probes
- fermentation, environmental and ecological studies




Surface Science

- UHV-TPD
- SIMS
- end point detection in ion beam etch
- elemental imaging - surface mapping



Plasma Diagnostics

- plasma source characterization
- etch and deposition process reaction kinetic studies
- analysis of neutral and radical species



Vacuum Analysis

- partial pressure measurement and control of process gases
- reactive sputter process control
- vacuum diagnostics
- vacuum coating process monitoring

Role of the reactive sputtering deposition power in the phase control of cobalt oxide films

Nilton Francelosi Azevedo Neto,¹ Douglas M. G. Leite,² Paulo N. Lisboa-Filho,¹ and José H. D. da Silva^{1,a)}

¹Faculdade de Ciências, Universidade Estadual Paulista, Bauru, São Paulo 17033-360, Brazil

²Laboratório de Plasmas e Processos—LPP, Instituto Tecnológico de Aeronáutica, São José dos Campos, São Paulo 12228-900, Brazil

(Received 3 July 2018; accepted 25 October 2018; published 14 November 2018)

The influence of the reactive magnetron sputtering deposition power on determining the stoichiometry and structure of cobalt oxide polycrystalline films is investigated using experimental and simulated data. Direct current discharges with powers in the 80–240 W range are tested using a metallic Co target and an Ar + O₂ plasma. X-ray diffraction results show that lower deposition powers favor the spinel Co₃O₄ phase, while higher powers produce films presenting the rocksalt CoO phase. Computer simulations indicate that lower power processes occur in the poisoned target regime, while higher power depositions favor the metallic target regime. Consistent with the simulations, oxygen optical emissions (O^I = 777.3 nm) from the plasma show a significant decrease while the cobalt emissions (e.g., the Co^I = 340.5 nm line) are significantly increased when the deposition power is increased. The results show that the film stoichiometry and structure are directly related to the deposition power, at constant O₂ flow. *Published by the AVS.* <https://doi.org/10.1116/1.5046952>

I. INTRODUCTION

The cobalt oxides have demonstrated applications in solar cells,¹ photocatalysis,² solar water splitting cells,³ and gas sensors,⁴ which are used to generate electric power, hydrogen gas, and to treat water effluents using the sunlight. These applications have the potential to significantly favor the cleaning of the environment, so the search for new alternative ways to produce the cobalt oxides in large area panels is assuming bold interest. Besides, the applications of these oxides extend also to electrodes for lithium-ion batteries⁵ and device memristors.⁶

The main phases of the cobalt oxides are the cubic spinel Co₃O₄ and the rocksalt CoO, each having different applications. Films of these phases have been obtained by pulsed laser deposition (PLD),⁷ molecular beam epitaxy (MBE),⁸ and sputtering.^{9,10} The latter has the potential to produce homogeneous films over large areas,¹¹ but generally presents poorer control on stoichiometry, defects, and film structure than MBE or PLD.

Achieving better control and understanding of the reactive sputtering deposition process can contribute to the development of the large area applications of these oxides. Nevertheless, the physics and chemistry involved in reactive sputtering are complex and highly nonlinear. Some models have been developed with the purpose of explaining how different parameters affect the reactive sputtering. Berg's model¹² explains the influence of the main deposition parameters on the reactive sputtering processes. It considers the formation of compounds on the target's surfaces due to chemisorption reactions between the target and reactive gas. Depla's model¹³ includes implantation of the reactive gas on the target during the process. Based on these models, it is

possible to predict the main features of the sputtering deposition regimes. The metallic regime is characterized by low compound formation on the target and low partial pressure of the reactive gas, while in the poisoned regime the reactive gas partial pressure increases and the target is covered by compounds.¹⁴ The outputs of these models are important to properly choose the deposition conditions and then gain control onto the composition and other important parameters of the deposited films by reactive sputtering.

This investigation focuses on cobalt oxide thin films deposited onto fused silica (a-SiO₂) substrates by reactive direct current (DC) magnetron sputtering using different discharge powers. The aim is to control the phase of the deposited films by changing only the deposition power. Computational simulations are used to assist the choices of the deposition parameters and to analyze the experimental results.

II. EXPERIMENTAL AND SIMULATIONS DETAILS

Cobalt oxide films were deposited by DC reactive magnetron sputtering. A 99.95% purity metallic cobalt target, 75 mm diameter, 70 mm away from the grounded substrate was used. The DC deposition power was varied from 80 to 240 W. Experiments were performed by an Advanced Energy MDX500DC power generator. The target erosion track (due to the magnetron system) presented an internal diameter of 17 mm and an external diameter of 25 mm. The base pressure in a vacuum chamber was lower than 8×10^{-5} Pa. The flows of the 6N purity argon and oxygen gases were set to 40.0 and 5.0 sccm, respectively, for all depositions. The working pressure was kept at 0.67 Pa. The main deposition parameters are shown in Table I. The samples were deposited onto fused silica (a-SiO₂) substrates. This amorphous substrate was preferred in order to minimize the effects of substrate and emphasize the effects of the

^{a)}Electronic mail: jose.humberto@unesp.br

TABLE I. Discharge power, voltage, total current, and ionic flux on depositions of cobalt oxide films using DC magnetron reactive sputtering. The resulting film thicknesses and the mean deposition rate were also included.

Discharge power (W)	Bias voltage (V)	Current (mA)	Ion flux [ion/(cm ² s)] × 10 ¹⁷	Film thickness (nm)	Mean deposition rate (Å/s)
80	309	258	1.48	260 ± 20	0.6
120	317	375	2.15	740 ± 70	2.7
160	358	444	2.54	1740 ± 40	9.0
170	344	490	2.80	820 ± 40	9.1
180	351	509	2.91	440 ± 50	10.5
200	366	542	3.10	438 ± 40	14.6
240	358	665	3.81	590 ± 20	19.6

discharge on the film structure and composition. The substrate temperature, 200 °C, was monitored during and after depositions using a thin K-type thermocouple wire placed in a position equivalent to the deposited film. The thicknesses of the films were measured after depositions with the help of a Veeco DekTak 150 profilometer. The average deposition rates were determined using the measured thickness and the deposition times, while the instant deposition rates were measured *in situ* using an Inficon FTS 2400 quartz crystal monitor. The different instant rates were measured in the same experiment by the sequential variation of the deposition power. The stabilization time after each power change was 5 min. The material density (6.44 g/cm³), acoustic impedance ($Z = 2.144 \times 10^6 \text{ g cm}^{-2} \text{ s}^{-1}$), and Z-factor to quartz (0.412) of CoO were used when performing all the growth rate measurements.

The ion flux [ion/(cm² s)] impinging on the target surface is defined as¹⁴

$$J_I = \frac{I}{e(1 + \gamma_e)A_t}, \quad (1)$$

where I is the measured discharge current, e is the elementary charge, γ_e is the electron yield, and A_t is the track area (10 cm²).

The structural analysis of the films by x-ray diffraction (XRD) is performed in a PANalytical Empyrean with CuK α ($\lambda = 1.54060 \text{ \AA}$) radiation, using $\theta-2\theta$ goniometer configuration in the 15° to 80° range with 0.01° step size. The crystallite sizes are estimated using Scherrer's formula.¹⁵ Computer simulations are performed to give insights about the deposition process. Using different softwares, the energy of the species arriving to the substrate and the characteristics of the reactive process are estimated.

The deposition regime and the target condition were analyzed using the Reactive Sputter Deposition Software, RSD2013.¹⁶ The simulation is based on reactive sputtering models developed by Berg and Nyberg¹² and Depla *et al.*¹⁶ The simulations were performed using the steady state method. Different sets of parameters are chosen to represent the experimental conditions in the RSD simulations. For each

deposition power, the target area ($A_t = 10 \text{ cm}^2$), substrate area ($A_s = 550 \text{ cm}^2$), pump speed ($S = 160 \text{ L/s}$), Ar pressure ($P_{\text{Ar}} = 0.43 \text{ Pa}$), temperature (300 K), and sticking coefficients ($\alpha_t = 0.6$, $\alpha_s = 0.8$) are kept constant, while the discharge current and sputtering yields are changed. The discharge current is taken directly from the experiment, while the sputtering yields as a function of the target composition and discharge voltage are established using the published experimental data (pure Co) and simulated values using the Transport of Ions in Matter (TRIM)¹⁷ software (oxides), as explained in the sequence.

In order to follow the experimental variations of the deposition power, the discharge current and the sputtering yields of the metal and compound are supplied to the RSD program. The change in the target potential in the different discharge powers has an indirect effect, due to changes in the sputtering yields. The calculation of the sputtering yields is not simple to perform accurately,^{18,19} especially for the metallic oxides.^{20–22} For this reason, we have used the measured value of sputtering yield of the pure Co, corresponding to normal incidence 300 eV Ar⁺ ions, reported by Laegreid and Wehner²³ ($Y_{\text{Co}} = 0.81$). This is very close to the conditions we have (a cathode voltage of 310 eV).

Concerning the sputtering yields of the oxides, as the experimental results of the cobalt oxides are not found for this energy range, we have used the SRIM simulations. These were performed by inserting the corresponding values of the binding energies for Co and O, which were calculated according to the simple model proposed by Malherbe *et al.*²¹ based on Pauling formalism. This procedure is expected to give more accurate values of the sputtering yields²⁰ than the regular calculation proposed in the TRIM program using just the binding energies of bulk Co and of the O₂ molecule. However, it is important to bear in mind that this is just an estimation so just the qualitative features of the results obtained from the RSD software should be considered in the present case.

A rough estimation of the kinetic energy of particles arriving to the substrate was performed using the TRIM (Refs. 17 and 24) program. This was made in order to get an insight about the physical processes occurring during the depositions. The calculations were performed in three steps. In the first step, the collisions of the ions with the target are analyzed. The kinetic energy of the Ar⁺ ion collision with the target was set with the potential energy originated from the full target voltage. Concerning the O₂ collisions, we have assumed molecule dissociation during impacts with the target, so half of the energy target potential was attributed to atomic oxygen collisions. This step was performed using the "Surface Sputtering" method of the TRIM program and resulted in the estimation of the energies of the species emerging from the target. In the second step, using the "Quick Calculation of Damage," the energies of Ar, O, and Co emerging from the target were used as input parameters in the transport through the gas in order to estimate the energy particles arriving to the substrate. Finally, the collisions of energetic species with the growing film surface are analyzed using the "Kinchen Pease" routine in TRIM.

The optical emissions from the plasma are acquired using an Avantes ULS2048, 3 channel spectrometer System, with optical fiber attachment, in the 260–1010 nm range. The emission lines were identified using the USA National Institute of Standards (NIST) atomic spectra database.²⁵

III. RESULTS AND DISCUSSION

In order to analyze the role of the deposition power in the growth of cobalt oxide films, characterizations using x-ray diffraction and optical emission from the plasma species during growth are presented in the sequence. The results are then discussed with the help of computer simulations.

A. X-ray diffraction

The crystalline phases present in cobalt oxide films deposited onto silica glass at different sputtering powers were analyzed using XRD. Figure 1(a) shows the diffraction pattern characteristics of polycrystalline films for all samples studied in this work.

The diffraction patterns from samples grown using low discharge powers (80, 120, and 160 W) show only cubic spinel Co_3O_4 phase related peaks—space group $Fd-3m$ (JCPDS No. 42-1467). On the other hand, the patterns from the samples grown at higher discharge powers (180, 200, and 240 W) show only rocksalt CoO diffraction peaks—space group $Fm-3m$ (JCPDS No. 48-1719). In between, the diffraction pattern from the sample grown at 170 W shows predominant Co_3O_4 phase peaks and some lower intensity peaks associated with the CoO phase, evidencing a phase mixing.

The 2θ plots around the Co_3O_4 (311) and CoO (111) peaks are shown in Fig. 1(b). These peaks, according to JCPDS No. 42-1467 and JCPDS No. 48-1719, are expected to occur at $2\theta = 36.853^\circ$ and $2\theta = 36.492^\circ$, respectively, as indicated with dashed vertical lines. From this plot, it is possible to notice the influence of the phase change on these nearby peaks.

Back to Fig. 1(a), the relative intensities of the observed diffraction peaks, when compared to those reported for the randomly orientated powders (JCPDS Nos. 42-1467

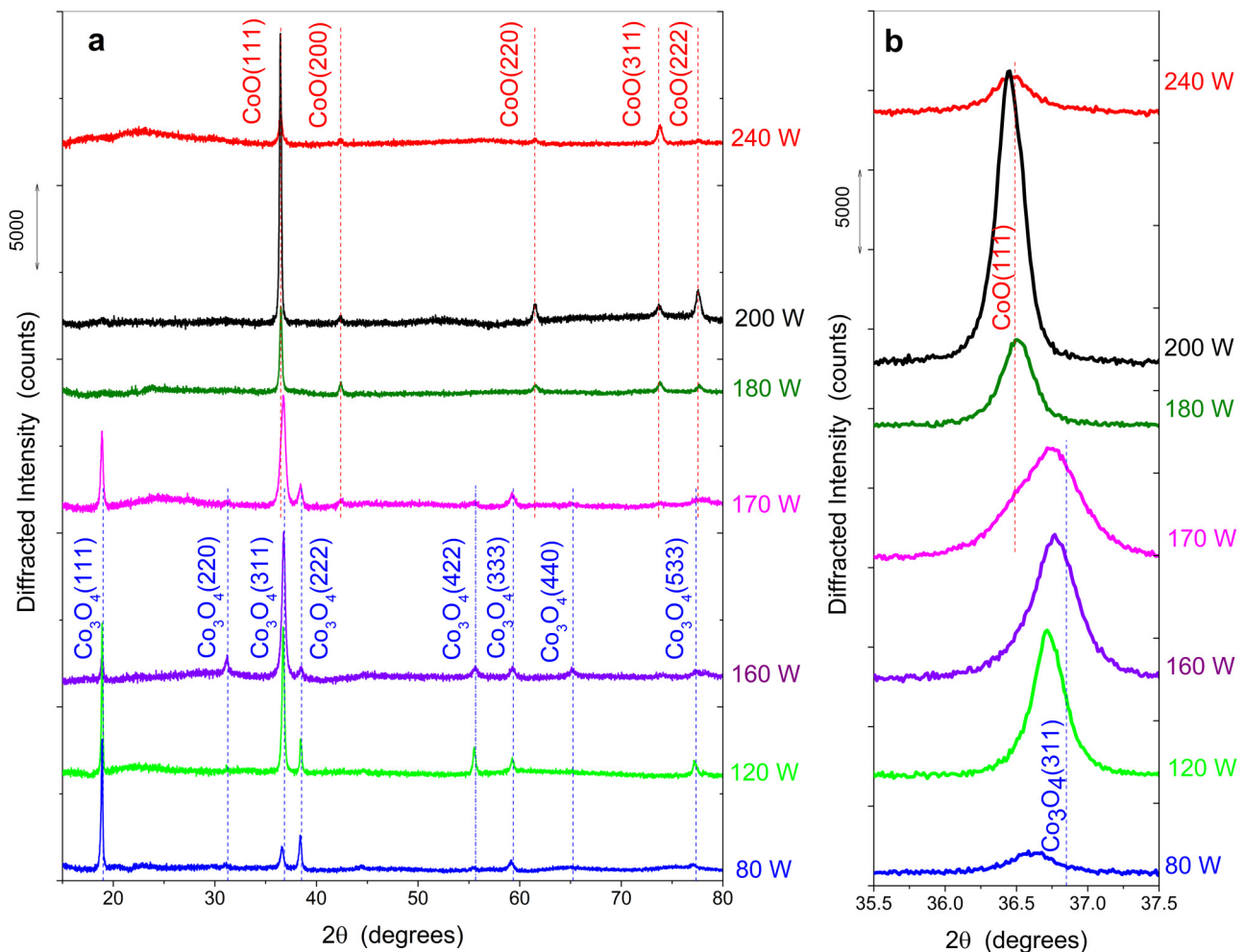


FIG. 1. (a) θ – 2θ diffraction pattern from cobalt oxide films deposited onto fused silica (a-SiO_2) substrate corresponding to different deposition powers. The labels of the peaks related to CoO are placed on the top (red labels) and marked with dashed red lines (JCPDF #42-1467), while the peaks related to Co_3O_4 are placed in the middle (blue labels) and marked with blue dotted lines (JCPDF #48-1719); (b) detail of the diffraction peaks related to Co_3O_4 (311) and CoO (111) planes.

and 48-1719), clearly indicate the presence of strong crystalline texture of both Co_3O_4 and CoO phases. It is possible to note that the peak intensities of the $\{220\}$ planes of the tetraoxide are much weaker in the studied films than expected. A similar trend is observed for both $\{200\}$ and $\{220\}$ in the monoxide. These facts, besides the $\theta-2\theta$ geometry used in the experiment, evidence that the preferential orientation of crystallites in which the $[111]$ and $[311]$ axes are perpendicular to the surface of the substrates on both cases (Co_3O_4 and CoO phases). Yamamoto *et al.*⁹ reported that the $[111]$ orientation texture tendency is also observed in Co_3O_4 films deposited by sputtering of a Co_3O_4 target when the substrate temperatures are above 300°C and especially for temperatures in the 600°C range. The tendency to this orientation of crystallites for such different deposition conditions on the amorphous silica substrates suggests that some dominant physical reason as the higher packing density of the (111) planes in the cubic lattice, associated with the small Si–O bonding distance of the silica glass substrate, or a higher velocity of growth in one direction (caused, for example, by surface energy minimization) may occur in this case. This is an interesting question for future experimental and theoretical investigations about this material.

In addition to the texture effects, most of the diffraction peaks observed in Fig. 1(a) occur in lower 2θ values when compared to the respective JCPDS data file. Consequently, the studied films hold large positive strains when deposited using powers lower or equal to 170 W, and small strains when prepared at 180 W and higher, as shown in Table II. Several studies show that ionic bombardment can be associated with phase changes, texture effects, and strain in the lattice in films produced by sputtering.^{26,27} The effects of ionic bombardment will be analyzed later in this section using computational simulations.

TABLE II. Measured d-spacing, strain, full-width at half-maximum (FWHM), and the estimated crystallite size of the Co_3O_4 and CoO phases corresponding to the (111) diffraction peaks. The strain was determined taking the data from JCPDF #42-1467 and JCPDF #48-1719 as references for the unstrained lattices. The lattice parameters of the unstrained Co_3O_4 ($a = 0.8083$ nm) and CoO ($a = 0.4261$ nm) can also be found on these JCPDF data files. The lattice parameters and crystallite sizes are estimated using Scherrer's formula (Ref. 15).

Discharge power (W)	Predominant phase	Lattice constant (nm)	(111)		Estimated crystallite size (nm)	
			spacing (\AA)	Strain (%)		
80	Co_3O_4	0.8132	4.695	0.60	0.181	48.9
120	Co_3O_4	0.8123	4.690	0.51	0.148	73.4
160	Co_3O_4	0.8125	4.691	0.52	0.251	36.7
170	Mix	0.8132	4.695	0.60	0.271	36.7
180	CoO	0.4259	2.459	-0.04	0.262	30.5
200	CoO	0.4264	2.462	0.10	0.226	38.1
240	CoO	0.4263	2.461	0.06	0.307	30.4

B. Simulations of the deposition regime

The RSD2013 software was used to simulate the characteristics of the reactive discharge. The oxygen partial pressures were simulated for each discharge power, while the O_2 supply was varied from 0 to 8 sccm, as shown in Fig. 2(a). Focusing on the oxygen flow effectively used in the depositions (5.0 sccm), marked as a dashed vertical line, it can be observed that lower powers favor higher oxygen partial pressure, in a regime where a linear dependence is observed between oxygen pressure and oxygen flow. This linear dependence is a clear characteristic of the poisoned growth regime, in which the target and chamber surfaces are completely contaminated by oxygen, leading to the formation of an oxide layer onto them, i.e., the target surface is mainly composed by cobalt oxide. On the other hand, the increase of the discharge power produces a significant and continuous decrease of the O_2 partial pressure and a shift of the curves to a nonlinear regime at 5 sccm. This behavior is a characteristic of the transition regime (poisoned to the metallic regime), where a mixture of pure metallic Co and Co oxide composes the target surface.

The simulation of the metal fraction in the target shows that the composition of the target surface also has a

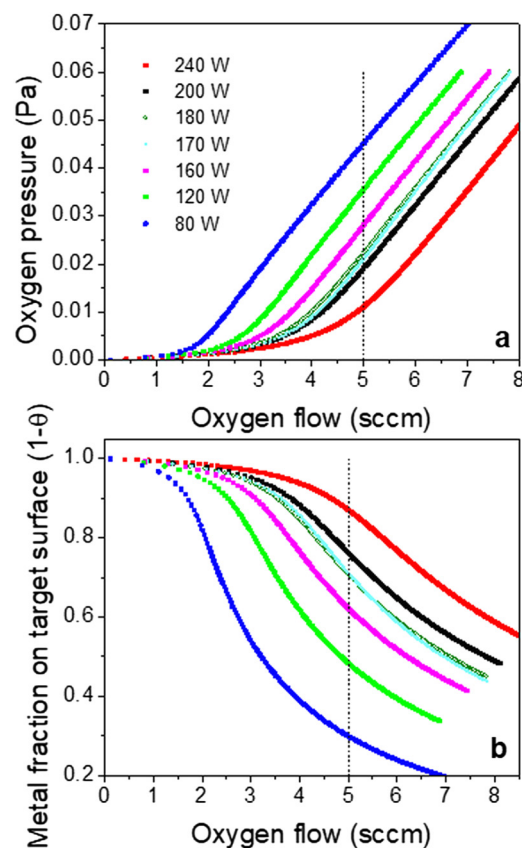


Fig. 2. (a) Oxygen partial pressure in the deposition process as a function of the oxygen gas flow into the chamber as simulated by RSD program. In this diagram, θ represents the fraction of the target covered by the compound and $1 - \theta$ represents the metallic fraction remaining on the target; (b) metal fraction, or oxide-free fraction, of the target surface. Calculations are performed for each value of the discharge power. The dotted vertical lines correspond to the oxygen flow used in the present experiment (5 sccm).

significant influence on the discharge power [Fig. 2(b)]. The simulated results of the metal fractions in the target for the different discharge powers used in this work are shown in Fig. 2(b). It is clear that, for 5 sccm oxygen flow, higher discharge powers result in higher steady state metal fractions, tending to the metallic deposition regime.

For example, for DC power equal or above 200 W, it is expected that at least 80% of the target surface area is composed of metallic Co. This condition results in stronger optical emissions from cobalt as measured during sputtering and shown in Fig. 3(a). However, at lower discharge powers, the metallic target fraction decreases, and thus the deposition processes tend to the poisoned regime.

The effects of the discharge power on the main optical emissions lines of the plasma are shown in Fig. 3(a). The plasma emission line at 777.3 nm (triangles), associated with oxygen $3p^5P \rightarrow 3s^5S$ transitions,^{25,28} is related to the dissociative excitation of the oxygen molecules ($e^- + O_2 \rightarrow O^I + O + e^-$).²⁸ A weaker line at 844.6 nm, related to $O^I[3p^3P \rightarrow 3s^3S]$ emissions²⁸ (not shown), is present in the emission spectra. The intensities associated with this line are 0.14 ± 0.03 of those corresponding to the

777.3 nm line, in the analyzed power range. The intensities of the oxygen emissions follow a trend similar to the Ar^I line at 826.3 nm. The decrease in the intensities of both emissions starting at 160 W and becoming more intense at higher powers is related to an increase of the Co emissions. Now looking to Co emissions [Fig. 3(a)], the increase in the discharge power leads to a strong increase of optical emission intensity associated with the cobalt $4p(4F^o) \rightarrow 4(4F)$ transitions at 340.5 nm (Ref. 25) evidencing the metallic regime for discharge powers above 180 W. Consequently, the chemical getter effect of the Co is likely to increase and cause the O depletion with the increase of the discharge power. While the decrease in the intensity of O is probably related to this depletion of O^I, the decrease in the Ar emissions is likely to be due to the competition for the energetic electrons in the plasma.

The dependence of the deposition rate on the discharge power is shown in Fig. 3(b). Different curves correspond to the mean deposition rates, determined from the thicknesses measured after the depositions (black squares), and to the instant deposition rates, obtained from deposition tests by using a quartz crystal microbalance. The latter were measured in two situations: increasing (triangles) and decreasing (circles) the deposition power using the same deposition parameters as in the films. At low deposition power (80 W), the measured rate is ~ 0.6 Å/s while at the highest power (240 W) the rate increases considerably up to ~ 20 Å/s. Even though the samples grown using DC power between 160 and 180 W are believed to reside in the transition target regime (poisoned to metallic), no significant hysteresis effect could be noticed on the growth rate as a function of the deposition power, while the other parameters are fixed. The smoother variation of the mean film growth rate, determined after the growth, as compared to the instant rate measurements, determined with the quartz crystal microbalance, can be due to a combination of factors. Among these, we can mention the possibility of unstable plasma conditions in the transition region from metallic to poisoned modes, averaging effects during the long term growth, and the bigger target-substrate distance, the larger size of the substrate holder, and the higher substrate temperature during the regular growth.

The increase in the deposition rate observed in Fig. 3(b) could be expected, since higher deposition powers provide (i) an increase in the number of collisions of ions against the target surface, as confirmed by the increase of ion flux; (ii) an increase in the energy of the ion-target collisions, due to the increase of the target potential; and (iii) an important reduction in the fraction of oxide on the target surface (transition to metallic regime).

In order to support point (iii) discussed above, it is important to quantify that the sputtering yield of cobalt oxide is ~ 0.34 atoms/Ar⁺ ion, as estimated by TRIM calculations when considering Ar⁺ ions accelerated by the target voltage, while the cobalt sputtering yield is about ~ 0.81 atoms/Ar⁺ ion (at 300 eV), as measured by Laegreid and Wehner.²³ Besides, and since the reactive oxygen is abundant especially at low powers as depicted in Fig. 2(a),

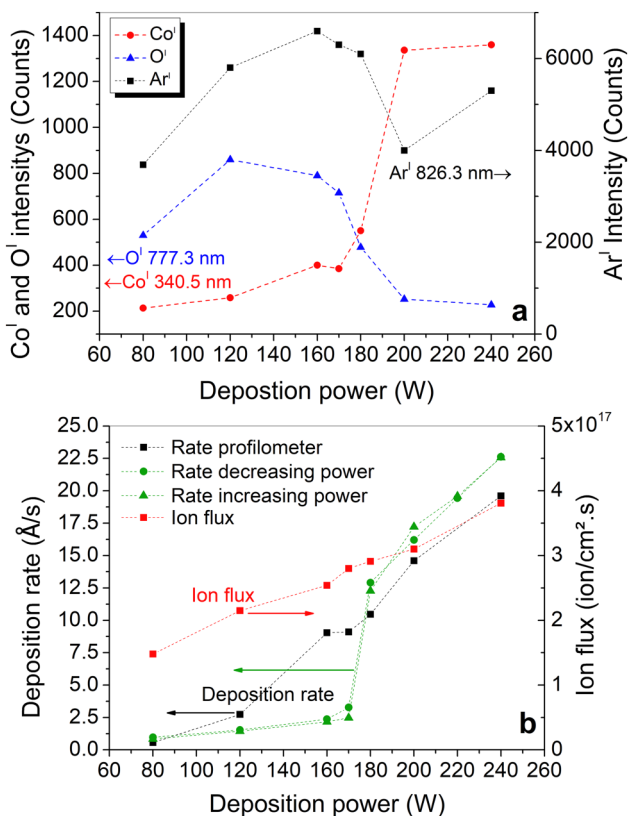


FIG. 3. Optical emission line intensities (a) from Co^I (340.5 nm), O^I (777.3 nm), and Ar^I (826.3 nm) for different powers in a DC plasma. The corresponding total pressure is 0.67 Pa. The constant O₂/Ar flows are 5.0 and 40 sccm, respectively. (b) Deposition rates measured with a quartz crystal balance with increasing (triangle) and decreasing (green circle) DC power during a test experiment. The average value of the growth rate for the films analyzed here (black squares), measured after growth with the help of a profile meter. The ion flux, Eq. (1), estimated using the deposition parameters is also shown (red squares).

the film formation is expected to be governed by the arrival of Co atoms to the substrate. In this way, the O ejected from the target is not important from the growth point of view, and the losses of ions and energy to provide its ejection will also hamper the film growth rate, mainly for the low deposition powers. The resemblance of the behavior of the Co emission, Fig. 3(a), with the growth rate, Fig. 3(b), confirms that the presence of Co is the main determinant of the film growth.

Summarizing the simulation results in the reactive sputtering process, there are strong indications that the samples grown using low discharge power occur in the poisoned target regime, where high oxygen partial pressure and low Co offering are established. This condition could be crucial to the formation of the Co_3O_4 phase observed in XRD for samples grown using DC powers above 170 W. Whereas the growth of the cubic CoO phase could be directly related to the high Co offer and relatively low oxygen pressure obtained for lower discharge power (<170 W), configuring the transition to the metallic target regime.

C. Calculation of the kinetic energies of species hitting the substrate

Besides the information gathered above about the offer of Co and O during the film growth process, it is also important to have information about the kinetic energies involved in depositions. The TRIM routine of the SRIM software¹⁷ was used to perform simulations of the collision processes of ions with the target and the substrate.

Considering first the collisions of Ar^+ and O^+ with the target, it is worth to recall that the average energies of the incident ions on the target depend on the target voltage in the plasma. As the mean free path of the ions in the working gas is of the order of centimeters, so much larger than the estimated cathode sheath, the measured target voltage was used as the acceleration potential for the collisions of Ar^+ impinging on the target. When considering the O_2^+ ions, due to impact dissociation, the energy of the individual O collisions with the target was set as the target voltage divided by two.²⁹ The collision process of Ar^+ and O^+ ions with the cobalt target results in the ejection of Co atoms (sputtered) and backscattered Ar and O. Due to the formation of compounds in the target, in low discharge powers the collisions of Ar^+ and O^+ were performed considering a CoO target.

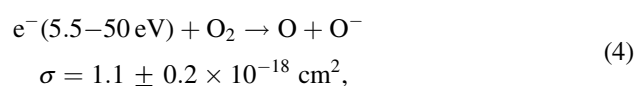
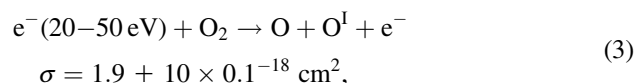
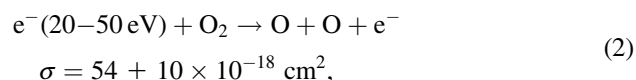
The average kinetic energies (K) of the particles leaving the target corresponding to depositions at 120 and 240 W show a clear increase of the ion kinetic energies due to the increase of discharge power. The energy of backscattered oxygen ion from the target is in the 22–30 eV range. Due to the electron attachment process, backscattered and sputtered oxygen can form O^- at the target surface. These negative ions are expected to be accelerated by the electric field and to collide with the forming thin film on the substrate with relatively high energies.²⁹ After particles leave the target, they cross the plasma region and reach the substrate. In this stage of the simulation, the kinetic energy of the particles that arrive on the substrate after crossing the plasma

region is calculated. The results show a decrease in the kinetic energy of the considered neutral atoms (Ar, Co, and O) and of the negatively charged oxygen after crossing plasma, as could be expected due to the losses produced by the collisions with the gas species. Simulation of the collisions of negative oxygen ions (330 eV) on the surface of the Co_3O_4 film reveals that these ions can create damage at Co and O sites.

Analyzing the optical emissions from O^{I} [Fig. 3(a)] and the simulations of the reactive process (Fig. 2), we can see that both indicate higher O_2 partial pressures in conditions related to the poisoned target regime, i.e., in lower powers. Under these conditions, one can expect also that the amount of O^- present in the plasma³⁰ should be much higher and, as shown in the collision simulations, produce subsurface implantation in the forming film. In this way, the O^- collisions can be correlated to the high tensile strains noticed in the films, since the higher strains occur at lower deposition powers [$P < 170$ W, Fig. 1(b)]. As the strain forming mechanisms directly influence some properties of films, especially those produced using plasmas, let us analyze this possibility in more detail.

According to literature reports, O^- ions can be produced in the plasma by low energy electron impact dissociation of the O_2 molecule,^{30–32} by collisions of plasma ions with the poisoned target,³³ and by electron transfer in the reflections of O^+ and O_2^+ colliding with the target.²⁹

Considering the electron impact dissociation of O_2 ,³¹ the formation cross sections of O, O^{I} (^1S), and O^- are



so, considering exclusively the electron impacts, it is possible to estimate the proportion $[\text{O}^-]/[\text{O}^{\text{I}}] \sim 0.6$ and also the proportion of the negatively ionized to the ground state O, $[\text{O}^-]/[\text{O}] \sim 0.02$.

The produced O^- ions are driven toward the substrates placed in the anode by the electric fields of the discharge, and can eventually produce defects and O interstitials in the films. Recalling that under the present conditions the mean free path for oxygen in the argon plasma (22 mm) is about one third of the target-substrate distance (70 mm), and setting the initial kinetic energies of O^- as 330 eV, equivalent to the full target potential, the simulations of O^- ions colliding with the Co_3O_4 film give a penetration range of the order of 10 Å, and approximately six vacancies can be produced by each incident ion. According to the detailed ion

energy analysis of the Ar/O₂ plasmas in sputtering by Welzel and Ellemer,²⁹ most O⁻ ions will have the full target potential when arriving to the substrate, and the present simulation shows that this is enough to produce subsurface damage with a considerable range. The estimated range of the implanted O is expected to be larger than the lattice parameter of the spinel Co₃O₄ lattice ($a = 0.8083$ nm). This indicates that subsurface implanted ions become entrapped during the film growth, and also the considerable number of vacancies produced by the energetic O may be responsible for the creation of Frenkel defects.^{34,35} These two could be responsible for the high positive strain (high swelling of the lattice) observed in the low power depositions. Counter-intuitively, this effect is not observed at higher powers. This apparent contradiction is attributed to the smaller O₂ pressure and the metallic target condition, which make the O⁻ production less likely at higher powers, so a much smaller positive strain and even slightly negative strain (lattice contraction) are observed.

One question that may arise is if the small quantity of O⁻ ions can be responsible for the observed strain. So, we discuss this in the sequence.

If we consider 0.1% of the O₂ available in the deposition chamber will produce one negatively charged O, this will correspond to a partial pressure of 2.7×10^{-5} Pa and to an O⁻ impingement flux of 7.4×10^{13} (ions/cm² s). This estimation is for a random movement of the O⁻, so it is likely to underestimate the preferential drive of ions by electric field heading ions to the substrate. These numbers correspond to the film deposited at 170 W, which is the one with the lowest O₂ partial pressure [extracted from Fig. 2(a), at 5 sccm]. We are using underestimated quantities because we are trying to establish a minimum amount of O⁻ collisions due to the present plasma conditions. In the 900 s deposition time of the film with the 0.91 nm/s deposition rate (expected to be the one with lower implantation/collision dose among the samples with higher strains), the film will have 6.6×10^{16} incident ions/cm². Considering the volume per square centimeter related to the film thickness (8.20×10^{-5} cm³), the implanted ion density should be 8.1×10^{20} ions/cm³ and this will correspond roughly to 1.6 at. % of implanted O in the film. Also, if the estimates made using SRIM are reasonable, each incident ion with the target potential energy could cause a few vacancies (~6/ion). Consequently, the damage produced by O⁻ collisions is expected to be large enough to produce the 0.6% strain observed, even if considerably less than 0.1% of the O₂ gas is ionized as O⁻.

Another point is to consider if there are another factors that can produce strain. One of these is the polycrystalline nature of the films. The presence of crystallites and their boundaries shall produce microstrains in the films due to intergrain forces. Nevertheless, these microstrains are expected to be compensated in the film volume averaging zero in the long range. They can produce diffraction peak broadening but no effective shift of the peaks.¹⁵ So, we shall seek for other long range factors.

Another source of long range strain could be the thermal stress. This is due to the different thermal expansion

coefficients of the Co₃O₄ film (6×10^{-6} K⁻¹) and silica glass substrate (5.5×10^{-7} K⁻¹) and the difference between the deposition and room temperatures (175 K). This will correspond to a tensile (positive) strain of ~0.1%, but this is parallel to the substrate surface. Considering the elastic regime, this shall correspond to compressive (negative) strain perpendicular to the substrate, which is the one observable in the $\theta-2\theta$ configuration of our diffractograms. In this way, we can rule out this as the possible source of strain in the films, reinforcing the argument in favor of the O⁻ collisions in producing the lattice swelling of the Co₃O₄.

Although these latter results are just indications and need further confirmation by more direct experimental evidence, they suggest an important issue related to the power of the sputtering discharge: low powers, favoring a higher concentration of oxygen species in the plasma, shall also be responsible for the strain in the films. This also suggests that higher substrate temperatures and higher total pressures should lower the strains in the films without changing the formed phase (Co₃O₄). TRIM simulations related to the collisions of neutral species also suggest that the collisions of Ar, Co, and uncharged O produced in the discharge with the substrates have much lower energies than O⁻ and will probably cause much weaker damage effects in the growing film surfaces. The corresponding energies are expected to be big enough to activate chemical reactions and produce surface rearrangement of particles.

IV. CONCLUSIONS

During the growth of cobalt oxide films by DC reactive magnetron sputtering, the discharge powers play a major role in determining the phase. While all deposition parameters are kept constant, especially the oxygen flow rate, the increase on the applied DC power is responsible for a phase change from the spinel Co₃O₄, at lower powers (80 to 160 W), to the rocksalt CoO at higher powers (180 to 240 W). The tetraoxide and the monoxide phases coexist on the films only on depositions at 170 W. The computer simulations suggest, and the optical emissions from the plasma confirm, that at lower powers the reactive gas partial pressure is higher and the metallic target is poisoned by the reactive gas. In contrast, when depositing at higher powers, the poisoned fraction of the target and the oxygen partial pressure decrease. These effects are caused by the higher sputtering rate of the metallic target at higher powers and the associated stronger chemical getter of the sputtered Co atoms on the reactive gas. No significant hysteresis behavior with the deposition power variation is noticed on the optical emissions or in the deposition rate for the set of parameters used.

It is proposed that the tensile strains observed in films, when deposited at relatively low powers, may be mainly attributed to the subsurface implantation of energetic O⁻ ions and to the creation of Frankel defects during film growth. An attenuation of these effects is expected for depositions at higher working pressures.

Being the reactive sputtering especially suited to the deposition of films over large substrate areas, the results attest

once more the potential of the technique in getting functional materials with reliable phase control and suited for different applications.

ACKNOWLEDGMENTS

The authors thank José R. R. Bortoleto and Angelo L. Gobbi for fruitful discussions and the TRIM (Ref. 16) and RSD2013 (Ref. 16) developers for providing free access to these very useful simulation programs. They acknowledge FAPESP (Grant No. 2017/18916-2), LNNano (No. LMF-15809), and FINEP (No. 01.13.0328.00) for the financial support.

- ¹C. Lohaus, J. Morasch, J. Brötz, A. Klein, and W. Jaegermann, *J. Phys. D: Appl. Phys.* **49**, 155306 (2016).
- ²C. Ravi Dhas, R. Venkatesh, D. David Kirubakaran, J. Princy Merlin, B. Subramanian, and A. Moses Ezhil Raj, *Mater. Chem. Phys.* **186**, 561 (2017).
- ³L. Liao *et al.*, *Nat. Nanotechnol.* **9**, 69 (2014).
- ⁴S. Vetter, S. Haffer, T. Wagner, and M. Tiemann, *Sens. Actuators B Chem.* **206**, 133 (2015).
- ⁵P. Poizot, S. Laruelle, S. Grugeon, L. Dupont, and J. M. Tarascon, *Nature* **407**, 496 (2000).
- ⁶K. Nagashima, T. Yanagida, K. Oka, M. Taniguchi, T. Kawai, J. S. Kim, and B. H. Park, *Nano Lett.* **10**, 1359 (2010).
- ⁷A. Matsuda, R. Yamauchi, D. Shiojiri, G. Tan, S. Kaneko, and M. Yoshimoto, *Appl. Surf. Sci.* **349**, 78 (2015).
- ⁸C. A. F. Vaz, V. E. Henrich, C. H. Ahn, and E. I. Altman, *J. Cryst. Growth* **311**, 2648 (2009).
- ⁹H. Yamamoto, S. Tanaka, and K. Hirao, *J. Appl. Phys.* **93**, 4158 (2003).
- ¹⁰C. L. Liao, Y. H. Lee, S. T. Chang, and K. Z. Fung, *J. Power Sources* **158**, 1379 (2006).
- ¹¹W. Graf, F. Brucker, M. Köhl, T. Tröscher, V. Wittwer, and L. Herlitzte, *J. Non Cryst. Solids* **218**, 380 (1997).
- ¹²S. Berg and T. Nyberg, *Thin Solid Films* **476**, 215 (2005).
- ¹³D. Depla, S. Heirwegh, S. Mahieu, and R. De Gryse, *J. Phys. D: Appl. Phys.* **40**, 1957 (2007).
- ¹⁴D. Depla, *Magnetrons, Reactive Gases and Sputtering* (Lulu, Morrisville, 2014).
- ¹⁵M. Birkholz, *Thin Film Analysis by X-Ray Scattering* (Wiley-VCH, Weinheim, 2006).
- ¹⁶K. Strijckmans and D. Depla, *J. Phys. D: Appl. Phys.* **47**, 235302 (2014).
- ¹⁷J. F. Ziegler, J. P. Biersack, and M. D. Ziegler, "TRIM-code in the SRIM-2013 package," see <http://www.srim.org>.
- ¹⁸P. Sigmund and C. Claussen, *J. Appl. Phys.* **52**, 990 (1981).
- ¹⁹K. Wittmaack, *J. Appl. Phys.* **96**, 2632 (2004).
- ²⁰M. P. Seah and T. S. Nunnery, *J. Phys. D: Appl. Phys.* **43**, 253001 (2010).
- ²¹J. B. Malherbe, S. Hofmann, and J. M. Sanz, *Appl. Surf. Sci.* **27**, 355 (1986).
- ²²H. Oechsner, H. Schoof, and E. Stumpe, *Surf. Sci.* **76**, 343 (1978).
- ²³N. Laegreid and G. K. Wehner, *J. Appl. Phys.* **32**, 365 (1961).
- ²⁴J. F. Ziegler, J. P. Biersack, and M. D. Ziegler, *SRIM – The Stopping and Range of Ions in Matter* (SRIM Co, Chester, MD, 2008).
- ²⁵A. Kramida, Y. Ralchenko, J. Reader, "Cobalt, oxygen and argon emission lines," NIST Atomic Spectra Database, retrieved September 12, 2018, see <http://physics.nist.gov/asd>.
- ²⁶S. Takayanagi, T. Yanagitani, and M. Matsukawa, *Appl. Phys. Lett.* **101**, 232902 (2012).
- ²⁷S. Mahieu, W. P. Leroy, K. Van Aeken, and D. Depla, *J. Appl. Phys.* **106**, 093302 (2009).
- ²⁸R. E. Walkup, K. L. Saenger, and G. S. Selwyn, *J. Chem. Phys.* **84**, 2668 (1986).
- ²⁹T. Welzel and K. Ellmer, *J. Vac. Sci. Technol. A* **30**, 61306 (2012).
- ³⁰A. Bogaerts, E. Bultinck, M. Eckert, V. Georgieva, M. Mao, E. Neyts, and L. Schwaederlé, *Plasma Process. Polym.* **6**, 295 (2009).
- ³¹J. W. McConkey, C. P. Malone, P. V. Johnson, C. Winstead, V. McKoy, and I. Kanik, *Phys. Rep.* **466**, 1 (2008).
- ³²D. Rapp and D. D. Briglia, *J. Chem. Phys.* **43**, 1480 (1965).
- ³³H. Toyoda, K. Goto, T. Ishijima, T. Morita, N. Ohshima, and K. Kinoshita, *Appl. Phys. Express* **2**, 126001 (2009).
- ³⁴J. W. Corbett, J. P. Karins, and T. Y. Tan, *Nucl. Instrum. Methods* **182–183**, 457 (1981).
- ³⁵W. Schilling, *J. Nucl. Mater.* **216**, 45 (1994).